J. Phase Equilib. Diffus.
https://doi.org/10.1007/s11669-025-01177-4

ORIGINAL RESEARCH ARTICLE

# Phase Equilibria in the V-Rich Region of the V-Si-B System at 1400 °C

**Weiguang Yang[1] · Georg Hasemann[2] · Mustafa Carrion Saldaña[3] · Bronislava Gorr[4] · Ruth Schwaiger[1,5] · Manja Krüger[2]**

Submitted: 11 August 2024 / in revised form: 18 January 2025 / Accepted: 29 January 2025


**Abstract** The phase equilibria in the V-rich region of the V-Si-B system, including the $V_8SiB_4$ phase, have been experimentally investigated. Eleven alloys with key compositions were produced by arc-melting or levitation-melting. The samples were then annealed at 1400 °C for 100/200/300 h under high vacuum condition. The as-cast and heat-treated alloys were investigated by scanning electron microscopy, electron backscatter diffraction, energy-dispersive x-ray spectroscopy and x-ray diffraction. The isothermal section at 1400 °C of the V-rich V-Si-B system was determined and compared with the one at 1600 °C. The determined isothermal section can be applied to the design of V-Si-B alloys.

✉ Weiguang Yang
w.yang@fz-juelich.de

Manja Krüger
manja.krueger@ovgu.de

[1] Institute of Energy Materials and Devices, Structure and Function of Materials (IMD−1), Forschungszentrum Jülich GmbH, Wilhelm−Johnen−Straße, 52428 Jülich, Germany

[2] Institute of Materials, Technologies and Mechanics, Otto−von−Guericke University Magdeburg, Universitätsplatz 2, 39106 Magdeburg, Germany

[3] Institute of Materials Technology, University Siegen, Paul−Bonatz−Strasse 9-11, 57076 Siegen, Germany

[4] Institute for Applied Materials−Applied Materials Physics (IAM−AWP), Karlsruhe Institute of Technology, Hermann−von−Helmholtz−Platz 1, 76344 Eggenstein−Leopoldshafen, Germany

[5] Chair of Energy Engineering Materials, Faculty 5, RWTH Aachen University, Templergraben 55, 52056 Aachen, Germany

**Keywords** energy dispersive spectrometry (EDS) · experimental phase equilibria · isothermal section · metallic alloys · ternary phase diagram · x-ray analysis

## 1 Introduction

Most high-temperature mechanical properties, e.g., high-temperature strength and creep resistance, can be correlated with the melting temperature of respective metals or alloys. Thus, similar to molybdenum-,[1–3] niobium-[4] and platinum-based alloys,[5] vanadium-based alloys are promising candidates for high-temperature structural applications due to the high melting temperature of vanadium and a comparatively low density. V-Si-B alloys are one of the most promising vanadium-based alloys because the addition of Si and B can improve the oxidation resistance by facilitating the formation of a protective silica layer primarily through the intermetallic phases such as $V_3Si$, $V_5Si_3$ and $V_5SiB_2$ .[6,7]

For alloy design and development, the phase diagram is one of the most important tools. The isothermal section of the V-Si-B system was first investigated at 1450 °C by Kudielka et al. [8] using X-ray diffraction (XRD) in 1957. Three alloys, which are located along $V_5B_3$-$V_5Si_3$ (Fig. 1), were produced via sintering at 1450 °C for 24 h under argon using powders of V (min. 99.86%), Si (min. 99.9%) and B (min. 96.35%).[8] Based on XRD, two three-phase phase fields were identified,[8] namely $\sim V_{0.7}B_{0.3}$-VB-$V_5SiB_2$ and $V_5SiB_2$-$V_3Si$-$D8_8$ (Fig. 1). The composition of $\sim V_{0.7}B_{0.3}$ phase, which was an unknown phase in 1957 for Kudielka et al. [8] was roughly estimated as 30 at.% B. One year later (in 1958), the crystal structure of the $\sim V_{0.7}B_{0.3}$ phase was determined by Nowotny and

Published online: 12 February 2025

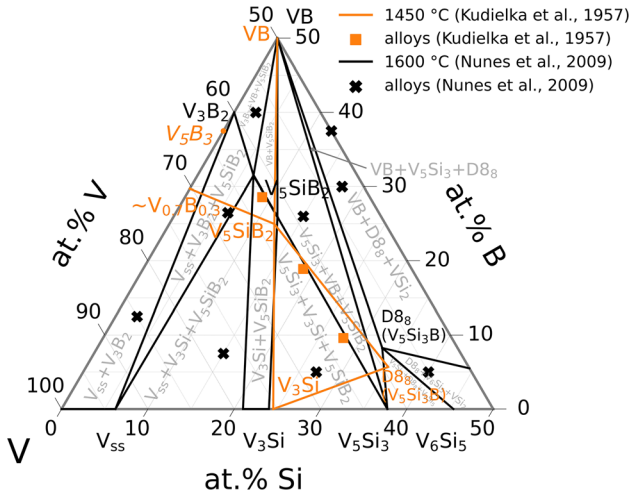


**Fig. 1** The partial isothermal section of the V-Si-B system at 1450 °C proposed by Kudielka et al. [8] in comparison to that at 1600 °C proposed by Nunes et al. [9]

Wittmann,[10] indicating that the $\sim V_{0.7}B_{0.3}$ phase actually was $V_3B_2$. Regarding the $D8_8$ phase, the defect enthalpies of formation of $D8_8$-$V_5Si_3$ unit cell, which were calculated using density functional theory (DFT),[11] indicate that the B atoms should interstitially be located at 2b sites. Because "$D8_8$" is also a Strukturbericht designation, the $D8_8$ phase is referred to as the $V_5Si_3B$ phase in the following.

The latest systematic experimental investigation of the isothermal section of the V-Si-B system was carried out by Nunes et al. [9] at 1600 °C in 2009. They produced the samples via arc-melting under argon followed by heat treatment at 1600 °C for 24 h and 72 h under high vacuum ($10^{-9}$ bar) using V (min. 99.75%), Si (min. 99.998%) and B (min. 99.95%). The samples were furnace cooled to room temperature at the end of the heat treatment. The composition of each phase in the samples investigated by Nunes et al. [9] (marked by "x" in Fig. 1) was measured by wavelength dispersive x-ray spectroscopy (WDS) using pure element standards. Based on the WDS results, the isothermal section of the V-Si-B system at 1600 °C in the V-VB-$VSi_2$ region of the V-Si-B system was proposed and is partially shown in Fig. 1. The observed binary V-Si and V-B phases (Fig. 1) are consistent with the investigated phase diagrams of V-Si [12–14] and V-B.[15] The B solubility in $V_{ss}$, $V_3Si$ and $V_5Si_3$ was found to be negligible, as was the Si solubility in $V_3B_2$ and VB.[9] Furthermore, the stabilities of the two ternary phases at 1600 °C, i.e.,$V_5Si_3B$ and $V_5SiB_2$, were confirmed, and a solubility range of the $V_5SiB_2$ phase was reported .[9]

Based on the isothermal section of the V-Si-B system at 1600 °C presented by Nunes et al. [9], V-9Si-13B (if not stated otherwise, all alloy compositions are given in at.% in this work) was chosen for a powder metallurgical (PM) processing route by Krüger et al. [7,16]. The PM processed V-9Si-13B, consisting of a continuous $V_{ss}$ matrix with embedded intermetallic phases $V_3Si$ and $V_5SiB_2$, showed great potential for high-temperature structural applications at around 900 °C.[7,16]

Recently, we have observed a new ternary phase, $V_8SiB_4$,[17] in the alloy V-5Si-9B annealed at 1400 °C. The new ternary phase has nearly the same composition as the $V_5SiB_2$ phase in the $V_{ss}$-$V_3B_2$-$V_5SiB_2$ phase field at 1600 °C but a different crystal structure.[17] The presence of the new ternary phase at 1400 °C indicates that there is indeed a difference between the isothermal sections of the V-rich V-Si-B system at 1400 °C and 1600 °C. In this work we have experimentally investigated the phase equilibria in the V-rich region of the V-Si-B system at 1400 °C. The microstructures were observed before and after different annealing times. The phase compositions and crystal structures were identified.

## 2 Experimental Methods

For producing samples, the raw materials (ChemPUR, Karlsruhe, Germany) were carefully weighed in the form of high-purity elemental turnings of V (99.7 wt.%) and granules of Si (99.99 wt.%) and B (99.0 wt.%) according to the nominal compositions of alloys listed in Table 1. The selection of alloy composition is based on the isothermal section of the V-Si-B system at 1600 °C (Fig. 1) [9] and the phase composition of $V_{ss}$ in the V-Si system at 1400 °C.[14] For each of the investigated V-Si-B alloy compositions having a B content less than 30 at.%, a 15 g button was produced by remelting five times in a conventional arc-melter under flowing argon gas, while for each of the investigated compositions having a B content greater than 30 at.%, a 10 g button was produced by remelting three times in a conventional arc-melter and then two times in a levitation melter under argon gas. A negligible weight loss (< 1 wt.%) indicates that the compositions after melting are very close to the nominal compositions. For confirmation, inductively coupled plasma optical emission spectroscopy (ICP-OES, iCAP 7600, Thermo Fisher Scientific, USA) was performed and the measured chemical compositions of the investigated

**Table 1** The nominal and chemical compositions of the alloys investigated in this work and the corresponding heat treatment duration at 1400 °C

| No. | Nominal composition, at.% | Actual chemical composition (according to ICP-OES), at.% | Heat treatment duration at 1400 °C, h |
|---|---|---|---|
| #1 | V-2Si-12B | V-2.1Si-11.5B | 0 (as-cast) |
| | | | 100 |
| | | | 200 |
| #2 | V-3Si-17B | V-2.9Si-17.6B | 0 (as-cast) |
| | | | 200 |
| | | | 300 |
| #3 | V-5Si-5B | V-5.2Si-4.7B | 0 (as-cast) |
| | | | 100 |
| | | | 200 |
| #4 | V-16.5Si-3.5B | V-16.7Si-3.5B | 0 (as-cast) |
| | | | 100 |
| | | | 200 |
| #5 | V-18.5Si-6.5B | V-17.9Si-6.1B | 0 (as-cast) |
| | | | 100 |
| | | | 200 |
| #6 | V-1Si-40B | V-1.0Si-42.0B | 0 (as-cast) |
| | | | 200 |
| | | | 300 |
| #7 | V-3Si-38B | V-2.8Si-38.7B | 0 (as-cast) |
| | | | 100 |
| | | | 200 |
| #8 | V-7Si-33B | V-7.2Si-33.7B | 0 (as-cast) |
| | | | 200 |
| | | | 300 |
| #9 | V-20Si-6.5B | V-20.4Si-6.3B | 0 (as-cast) |
| | | | 100 |
| | | | 300 |
| #10 | V-26Si-3B | V-25.5Si-3.4B | 0 (as-cast) |
| | | | 100 |
| | | | 200 |
| #11 | V-20Si-20B | V-22.2Si-17.1B | 0 (as-cast) |
| | | | 200 |
| | | | 300 |

alloys are shown in Table 1. Combustion analysis (Leco CS600, LECO, USA) was used to determine the carbon (C) content of the alloys. The as-cast buttons were cut in half by electrical discharge machining (EDM). One half was used to investigate the as-cast microstructure, while the other half was heat-treated at 1400 °C for 100 h under high vacuum ($1.5x10^{-5}$ mbar) and furnace cooled within 3 h below 200 °C. The annealing at 1400 °C for 100 h was repeated 2 or 3 times. The heat treatment times of the investigated alloys are listed in Table 1.

For metallographic preparation, the samples were cold-mounted (Expoy 2000, Cloeren Technology, Wegberg, Germany), and subsequently ground with SiC papers down to 2000 grit. The polishing was conducted with 15 µm, 6 µm, 3 µm and 1 µm diamond suspension, and finished with colloidal silica.

X-ray diffraction (XRD) measurements were performed on the polished bulk samples at room temperature using a diffractometer EMPYREAN (Malvern Panalytical, UK) or a diffractometer D8 ADVANCE (Bruker, USA) to identify the crystal structures of the phases. The lattice parameters of the phases were determined using the software GSAS-II [18] and the Pawley refinement,[19] in which the intensities of the calculated diffraction peaks do not depend on the atomic kinds and positions in the crystal structure. Except for the $V_8SiB_4$ phase, whose crystal structure was taken from recent work,[17] the corresponding crystal structures used for the XRD were taken from the Inorganic Crystal Structure Database (ICSD) [20] with the collection code 241937,[21] 87328,[22] 652506,[23] 652505,[23] 88317,[24] 44490[8] and 615658[25] for $V_{ss}$, $V_3Si$, tetragonal $V_5Si_3$, hexagonal $V_5Si_3$, $V_3B_2$, VB and $V_5SiB_2$ phases, respectively.

A Zeiss Merlin (Zeiss Microscopy, Oberkochen, Germany) scanning electron microscope (SEM) was used to observe the microstructures using the backscattered electron (BSE) mode. Furthermore, electron backscatter diffraction (EBSD, Oxford Instruments, UK) with a scanning step size smaller than 0.6 µm for the as-cast samples and smaller than 1 µm for the heat-treated samples was used to identify the phases by matching the backscatter Kikuchi patterns to the crystal structures of $V_{ss}$, $V_3Si$, $V_5Si_3$, $V_3B_2$, VB and $V_5SiB_2$ and obtain the phase mapping. Due to the similar crystal structure of the $V_5SiB_2$ and $V_8SiB_4$ phases, the $V_5SiB_2$ phase suggested by EBSD can be identified as the $V_8SiB_4$ phase in the EBSD phase mapping when the $V_8SiB_4$ phase was suggested by Energy-dispersive X-ray spectroscopy (EDS, X-Max 150, Oxford Instruments, UK) and XRD. In the case of coexistence of $V_5SiB_2$ and $V_8SiB_4$ phases, the crystal structures of both phases were used for matching the backscatter Kikuchi patterns.

After confirming the homogeneity of elemental distribution in every single phase using EDS mapping, EDS point measurements were performed to quantitatively determine the chemical compositions of phases. The AZtec software (Oxford Instruments, UK) was used to calculate the element amount in weight percent. Pure V, Si, and B were used as standard materials for the calibration of EDS. It should be noted that the quantitative detection of B using EDS is challenging because of the low electron density of B atoms (5 electrons per atom [26]), but can be achieved since no peak overlap with the V or Si EDS spectra exists (in contrast to the Mo $M_\zeta$-line of 0.193 keV and the B $K_\alpha$-line of 0.183 keV [27]). Furthermore, the B content of the B-containing phases investigated in this work is sufficiently high to be detected.

The phase area fraction was determined by EBSD, while the phase volume fraction was determined using the phase compositions and the phase molar volumes measured by EDS and XRD, respectively. For a three-phase alloy, using the measured composition of each phase $j$, $c_j^{Si}$ and $c_j^B$ in at.%, the phase molar fraction of each phase $f_j$ can be calculated by solving the following set of equations:

$$\begin{cases} \sum_j f_j = 1 \\ \sum_j f_j c_j^{Si} = c_{alloy}^{Si} \\ \sum_j f_j c_j^B = c_{alloy}^B \end{cases}, \quad \text{(Eq 1)}$$

where $c_{alloy}^{Si}$ and $c_{alloy}^B$ are the alloy compositions in at.%. For a three-phase alloy, the nominal alloy compositions (Table 2) were used in Eq 1. By contrast, for a two-phase alloy, the alloy composition, which fulfills the set of Eq 1 and is the closest to the nominal alloy composition, was used to calculate the phase molar fractions. The calculated phase molar fractions can be converted to the phase volume fractions using the phase molar volumes determined by XRD.

## 3 Results and Discussion

The microstructural evolution upon annealing at 1400 °C of the alloys investigated is presented in section 3.1. The evolution of phase area or volume fraction with increasing annealing time was used to confirm the equilibrium state of the alloys studied in this work. Then the isothermal section of the V-Si-B system at 1400 °C is proposed in section 3.2. To estimate the accuracy of the EDS analysis, the measured compositions of binary phases were compared to those reported in the binary V-Si and V-B systems in section 3.3.

### 3.1 Evolution of Microstructure and Phase Composition in Each Phase Field

#### *3.1.1 Phase Field of $V_{ss}$-$V_3B_2$*

The microstructure of the as-cast alloy V-2Si-12B consists of the $V_3B_2$ primary phase having a polygonal shape and the $V_{ss}$-$V_3B_2$ eutectic (Fig. 2a). After annealing at 1400 °C

**Table 2** Lattice parameters (Å) of phases in the as-cast and heat-treated (1400 °C) V − Si − B alloys

| No. | Alloy | Heat treatment time, h | $V_{ss}$, *Im*$\bar{3}$*m* | VB, *P4/mbm* | | | $V_3Si$, *Pm*$\bar{3}$*n* | $V_3B_2$, *P4/mbm* | | $V_5Si_3$, *I4/mcm* | | $V_5Si_3$, *P6*$_3$*/mcm* | | $V_5SiB_2$, *I4/mcm* | | $V_8SiB_4$, *I4/mcm* | |
|---|---|---|---|---|---|---|---|---|---|---|---|---|---|---|---|---|---|
| | | | a | a | b | c | a | a | c | a | c | a | c | a | c | a | c |
| #1 | V-2Si-12B | 0 (as-cast) | 3.026 | ... | ... | ... | ... | 5.732 | 3.026 | ... | ... | ... | ... | ... | ... | ... | ... |
| | | 100 | 3.029 | ... | ... | ... | ... | 5.741 | 3.031 | ... | ... | ... | ... | ... | ... | ... | ... |
| | | 200 | 3.026 | ... | ... | ... | ... | 5.738 | 3.030 | ... | ... | ... | ... | ... | ... | ... | ... |
| #2 | V-3Si-17B | 0 (as-cast) | 3.022 | ... | ... | ... | ... | 5.739 | 3.029 | ... | ... | ... | ... | ... | ... | ... | ... |
| | | 200 | 3.025 | ... | ... | ... | ... | 5.740 | 3.030 | ... | ... | ... | ... | ... | ... | 5.768 | 16.796 |
| | | 300 | 3.023 | ... | ... | ... | ... | 5.738 | 3.030 | ... | ... | ... | ... | ... | ... | 5.769 | 16.791 |
| #3 | V-5Si-5B | 0 (as-cast) | 3.022 | ... | ... | ... | ... | 5.738 | 3.031 | ... | ... | ... | ... | 5.769 | 10.765 | ... | ... |
| | | 100 | 3.023 | ... | ... | ... | 4.737 | ... | ... | ... | ... | ... | ... | ... | ... | 5.765 | 16.793 |
| | | 200 | 3.027 | ... | ... | ... | 4.739 | ... | ... | ... | ... | ... | ... | ... | ... | 5.769 | 16.799 |
| #4 | V-16.5Si-3.5B | 0 (as-cast) | 3.026 | ... | ... | ... | 4.736 | ... | ... | ... | ... | ... | ... | 5.767 | 10.737 | ... | ... |
| | | 100 | 3.026 | ... | ... | ... | 4.740 | ... | ... | ... | ... | ... | ... | ... | ... | 5.768 | 16.793 |
| | | 200 | 3.026 | ... | ... | ... | 4.739 | ... | ... | ... | ... | ... | ... | ... | ... | 5.769 | 16.799 |
| #5 | V-18.5Si-6.5B | 0 (as-cast) | 3.024 | ... | ... | ... | 4.730 | ... | ... | ... | ... | ... | ... | 5.785 | 10.772 | ... | ... |
| | | 100 | ... | ... | ... | ... | 4.736 | ... | ... | ... | ... | ... | ... | 5.786 | 10.766 | 5.781 | 16.781 |
| | | 200 | ... | ... | ... | ... | 4.736 | ... | ... | ... | ... | ... | ... | 5.781 | 10.776 | 5.780 | 16.770 |
| #6 | V-1Si-40B | 0 (as-cast) | 3.027 | 3.061 | 8.047 | 2.971 | ... | 5.742 | 3.030 | ... | ... | ... | ... | ... | ... | ... | ... |
| | | 200 | 3.040* | 3.060 | 8.046 | 2.977 | ... | 5.739 | 3.029 | ... | ... | ... | ... | ... | ... | 5.768 | 16.799 |
| | | 300 | 3.051* | 3.061 | 8.048 | 2.971 | ... | 5.739 | 3.029 | ... | ... | ... | ... | ... | ... | 5.766 | 16.818 |
| #7 | V-3Si-38B | 0 (as-cast) | 3.028 | 3.062 | 8.049 | 2.973 | ... | 5.732* | 3.019* | ... | ... | ... | ... | 5.775 | 10.744 | 5.760* | 16.813* |
| | | 100 | ... | 3.062 | 8.051 | 2.969 | 4.739* | 5.740 | 3.030 | ... | ... | ... | ... | 5.786 | 10.799 | 5.770 | 16.793 |
| | | 200 | ... | 3.062 | 8.047 | 2.971 | 4.736* | 5.739 | 3.029 | ... | ... | ... | ... | 5.787 | 10.761 | 5.768 | 16.786 |
| #8 | V-7Si-33B | 0 (as-cast) | 3.033* | 3.058 | 8.055 | 2.974 | 4.737 | ... | ... | ... | ... | ... | ... | 5.786 | 10.770 | ... | ... |
| | | 200 | 3.049* | 3.061 | 8.049 | 2.971 | 4.734 | 5.740 | 3.030 | ... | ... | ... | ... | 5.786 | 10.772 | ... | ... |
| | | 300 | 3.050* | 3.060 | 8.040 | 2.973 | 4.732 | 5.740 | 3.030 | ... | ... | ... | ... | 5.786 | 10.774 | ... | ... |
| #9 | V-20Si-6.5B | 0 (as-cast) | ... | ... | ... | ... | 4.730 | ... | ... | ... | ... | ... | ... | 5.784 | 10.772 | ... | ... |
| | | 100 | ... | ... | ... | ... | 4.731 | ... | ... | ... | ... | ... | ... | 5.785 | 10.770 | ... | ... |
| | | 300 | ... | ... | ... | ... | 4.730 | ... | ... | ... | ... | ... | ... | 5.787 | 10.776 | ... | ... |
| #10 | V-26Si-3B | 0 (as-cast) | ... | ... | ... | ... | 4.726 | ... | ... | 9.417 | 4.752 | ... | ... | 5.798 | 10.793 | ... | ... |
| | | 100 | ... | ... | ... | ... | 4.728 | ... | ... | 9.420 | 4.750 | 7.143* | 4.868* | 5.798 | 10.798 | ... | ... |
| | | 200 | ... | ... | ... | ... | 4.728 | ... | ... | 9.420 | 4.750 | 7.142* | 4.865* | 5.798 | 10.796 | ... | ... |
| #11 | V-20Si-20B | 0 (as-cast) | ... | 3.058 | 8.055 | 2.971 | 4.726 | ... | ... | 9.412 | 4.727 | ... | ... | 5.795 | 10.786 | ... | ... |
| | | 200 | ... | 3.062 | 8.050 | 2.971 | 4.727 | ... | ... | 9.423 | 4.757 | 7.147 | 4.872 | 5.798 | 10.793 | ... | ... |
| | | 300 | ... | 3.060 | 8.052 | 2.974 | ... | ... | ... | 9.422 | 4.738 | ... | ... | 5.797 | 10.791 | ... | ... |

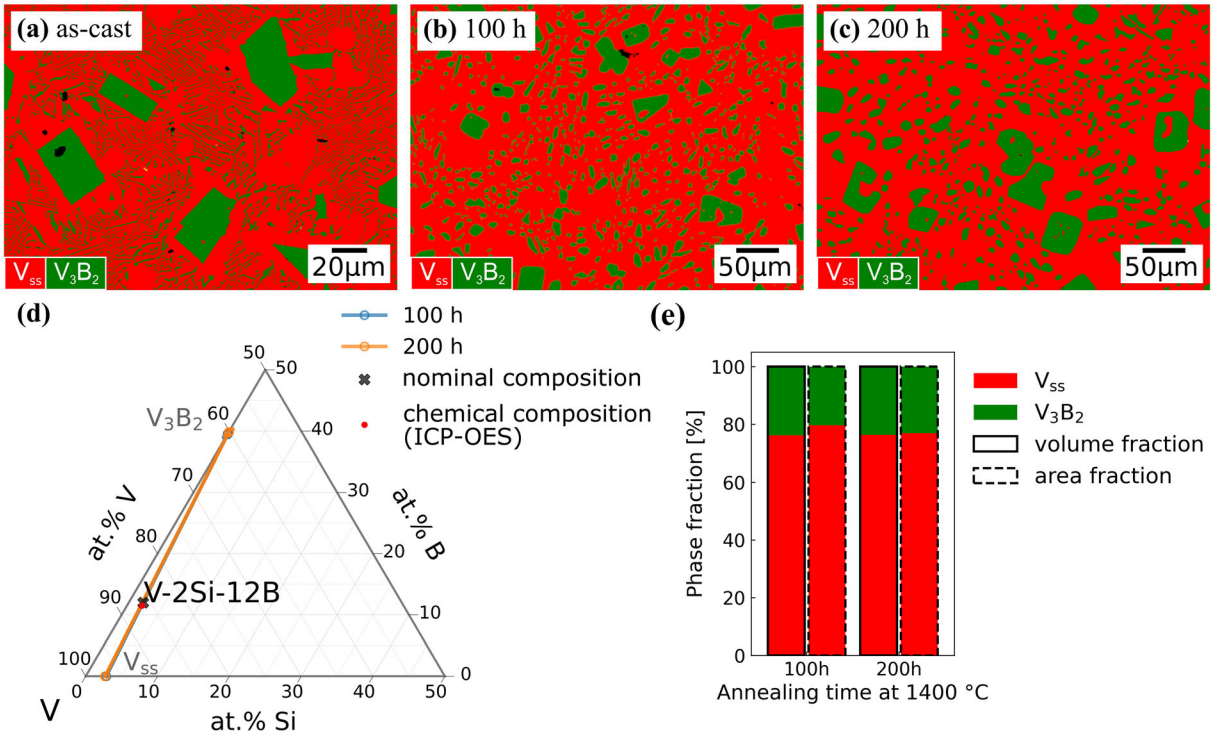


**Fig. 2** Experimental microstructures (EBSD phase mappings) of alloy V-2Si-12B in the (a) as-cast condition and after annealing for (b) 100 h and (c) 200 h. (d)The phase compositions measured by EDS (marked with open circles), where the error bars are plotted along the fixed B and Si contents for the standard deviations exceeding 0.3 at.% Si and B. (e) The evolution of phase volume and area fractions showing that the equilibrium state at 1400 °C was reached after 100 h

for 100 h, the corners of the polygon-shaped $V_3B_2$ phase were rounded, while the $V_{ss}$-$V_3B_2$ eutectic was replaced by the globular $V_3B_2$ phase distributed in the $V_{ss}$ phase (Fig. 2b). The microstructure after heat treatment at 1400 °C for 200 h is similar to the microstructure after 100 h (Fig. 2c). In agreement with the observed microstructures, the XRD results show that there are two phases present after annealing, i.e., the $V_{ss}$ phase and the $V_3B_2$ phase (Table 2). The EDS results of the annealed alloys V-2Si-12B (Table 3) are plotted in a ternary diagram (Fig. 2d), where the compositional position of alloy V-2Si-12B is located on the line connecting the $V_{ss}$ phase and the $V_3B_2$ phase. The change of each phase volume or area fraction does not depend on the annealing time (Fig. 2e). Therefore, after 100 h, the alloy V-2Si-12B must have reached the equilibrium state at 1400 °C, which confirms the $V_{ss}$-$V_3B_2$ phase field.

### *3.1.2 Phase Field of $V_{ss}$-$V_3B_2$-$V_8SiB_4$*

In the as-cast alloy V-3Si-17B, the VB primary phase is surrounded by the $V_3B_2$ phase, and the $V_{ss}$-$V_3B_2$ eutectic was observed (Fig. 3a). After 200 h of annealing at 1400 °C, the VB primary phase was no longer observed (Fig. 3b), which indicates the transformation of the VB primary phase into the $V_{ss}$ and $V_3B_2$ phases. The $V_{ss}$-$V_3B_2$ eutectic was replaced by the globular $V_3B_2$ phase and the newly formed $V_8SiB_4$ phase (Fig. 3b). The observed microstructure agrees well with the XRD results (Table 2). When the annealing time was increased to 300 h, no microstructural changes were observed (Fig. 3c). Correspondingly, the phase compositions measured by EDS after 200 h are almost identical to those after 300 h (Table 3 or Fig. 3d). The volume or area fraction of each phase did not change with increasing annealing time (Fig. 3e). Thus, it can be confirmed that 200 h is sufficient for the alloy V-3Si-17B to reach the equilibrium state at 1400 °C. The annealed alloys V-3Si-17B were used to determine the phase field of $V_{ss}$-$V_3B_2$-$V_8SiB_4$.

### *3.1.3 Phase Field of $V_{ss}$-$V_3Si$-$V_8SiB_4$*

Comparing the microstructures of the as-cast and annealed (1400 °C/100 h) alloy V-5Si-5B (Fig. 4a and b), it can be seen that the dendritic $V_{ss}$ primary phase and the $V_{ss}$-$V_3B_2$ and the $V_{ss}$-$V_5SiB_2$ eutectics had vanished after annealing. In agreement with the observed annealed microstructures, the XRD results show that the annealed alloys consist of $V_{ss}$, $V_3Si$ and $V_8SiB_4$ phases (Table 2). The newly formed $V_8SiB_4$ phases may have been transformed from the

**Table 3** Composition of phases (at.%) measured by EDS in the heat-treated (1400 °C) V-Si-B alloys

| No. | Alloy | Heat treatment time, h | $V_{ss}$ | | VB | | $V_3Si$ | | $V_3B_2$ | | $V_5Si_3$ | | $V_5SiB_2$ | | $V_8SiB_4$ | |
|---|---|---|---|---|---|---|---|---|---|---|---|---|---|---|---|---|
| | | | Si | B | Si | B | Si | B | Si | B | Si | B | Si | B | Si | B |
| #1 | V-2Si-12B | 100 | 2.8 ± 0.1 | 0 | ... | ... | ... | ... | 0 | 39.5 ± 0.5 | ... | ... | ... | ... | ... | ... |
| | | 200 | 2.7 ± 0.1 | 0 | ... | ... | ... | ... | 0 | 39.8 ± 0.5 | ... | ... | ... | ... | ... | ... |
| #2 | V-3Si-17B | 200 | 3.8 ± 0.1 | 0 | ... | ... | ... | ... | 0 | 40.1 ± 0.5 | ... | ... | ... | ... | 6.4 ± 0.1 | 31.3 ± 0.7 |
| | | 300 | 3.8 ± 0.1 | 0 | ... | ... | ... | ... | 0 | 39.3 ± 0.6 | ... | ... | ... | ... | 6.6 ± 0.2 | 29.7 ± 0.8 |
| #3 | V-5Si-5B | 100 | 4.1 ± 0.1 | 0 | ... | ... | 18.9 ± 0.1 | 0 | ... | ... | ... | ... | ... | ... | 6.5 ± 0.2 | 30.8 ± 1.2 |
| | | 200 | 3.9 ± 0.1 | 0 | ... | ... | 18.9 ± 0.1 | 0 | ... | ... | ... | ... | ... | ... | 6.6 ± 0.2 | 30.3 ± 0.5 |
| #4 | V-16.5Si-3.5B | 100 | 4.1 ± 0.1 | 0 | ... | ... | 19.4 ± 0.3 | 0 | ... | ... | ... | ... | ... | ... | 6.5 ± 0.2 | 31.4 ± 0.8 |
| | | 200 | 3.3 ± 0.3 | 0 | ... | ... | 19.2 ± 0.2 | 0 | ... | ... | ... | ... | ... | ... | 6.6 ± 0.2 | 30.5 ± 1.1 |
| #5 | V-18.5Si-6.5B | 100 | ... | ... | ... | ... | 20.1 ± 0.3 | 0 | ... | ... | ... | ... | 11.5 ± 0.3 | 22.9 ± 1.5 | 6.9 ± 0.3 | 30.0 ± 1.9 |
| | | 200 | ... | ... | ... | ... | 19.8 ± 0.1 | 0 | ... | ... | ... | ... | 11.1 ± 0.3 | 24.5 ± 1.1 | 6.6 ± 0.1 | 31.0 ± 0.6 |
| #6 | V-1Si-40B | 200 | ... | ... | 0 | 49.8 ± 0.5 | ... | ... | 0 | 39.6 ± 0.9 | ... | ... | ... | ... | 6.6 ± 0.3 | 30.6 ± 1.0 |
| | | 300 | ... | ... | 0 | 50.1 ± 0.5 | ... | ... | 0 | 40.1 ± 0.5 | ... | ... | ... | ... | 6.5 ± 0.1 | 31.2 ± 0.7 |
| #7 | V-3Si-38B | 100 | 1.7 ± 0.6 | 0 | 0 | 50.3 ± 0.6 | 20.9 ± 0.2 | 0 | 0 | 40.4 ± 0.7 | ... | ... | 10.9 ± 0.2 | 25.2 ± 1.1 | 6.6 ± 0.4 | 31.7 ± 1.1 |
| | | 200 | ... | ... | 0 | 49.8 ± 0.3 | ... | ... | 0 | 40.7 ± 0.7 | ... | ... | 10.8 ± 0.2 | 25.8 ± 0.8 | 6.6 ± 0.1 | 31.9 ± 0.6 |
| #8 | V-7Si-33B | 200 | ... | ... | 0 | 50.5 ± 0.4 | 22.8 ± 0.2 | 0 | 0 | 40.5 ± 1.0 | ... | ... | 11.1 ± 0.3 | 25.3 ± 1.0 | ... | ... |
| | | 300 | ... | ... | 0 | 50.6 ± 0.4 | 23.2 ± 0.1 | 0 | 0 | 40.7 ± 0.7 | ... | ... | 11.1 ± 0.3 | 25.7 ± 0.8 | 6.7 ± 0.2 | 31.8 ± 0.6 |
| #9 | V-20Si-6.5B | 100 | ... | ... | ... | ... | 21.5 ± 0.1 | 0 | ... | ... | ... | ... | 11.3 ± 0.4 | 25.3 ± 1.0 | ... | ... |
| | | 300 | ... | ... | ... | ... | 21.8 ± 0.1 | 0 | ... | ... | ... | ... | 11.1 ± 0.2 | 25.5 ± 0.9 | ... | ... |
| #10 | V-26Si-3B | 100 | ... | ... | ... | ... | 23.5 ± 0.1 | 0 | ... | ... | 35.2 ± 0.2 | 0 | 12.1 ± 0.1 | 23.9 ± 0.8 | ... | ... |
| | | 200 | ... | ... | ... | ... | 23.6 ± 0.1 | 0 | ... | ... | 35.2 ± 0.1 | 0 | 12.4 ± 0.2 | 22.3 ± 1.0 | ... | ... |
| #11 | V-20Si-20B | 200 | ... | ... | 0 | 50.8 ± 0.7 | ... | ... | ... | ... | 35.6 ± 0.2 | 0 | 12.0 ± 0.2 | 24.4 ± 0.8 | ... | ... |
| | | 300 | ... | ... | 0 | 49.9 ± 0.6 | ... | ... | ... | ... | 35.4 ± 0.2 | 0 | 12.0 ± 0.2 | 24.6 ± 0.8 | ... | ... |

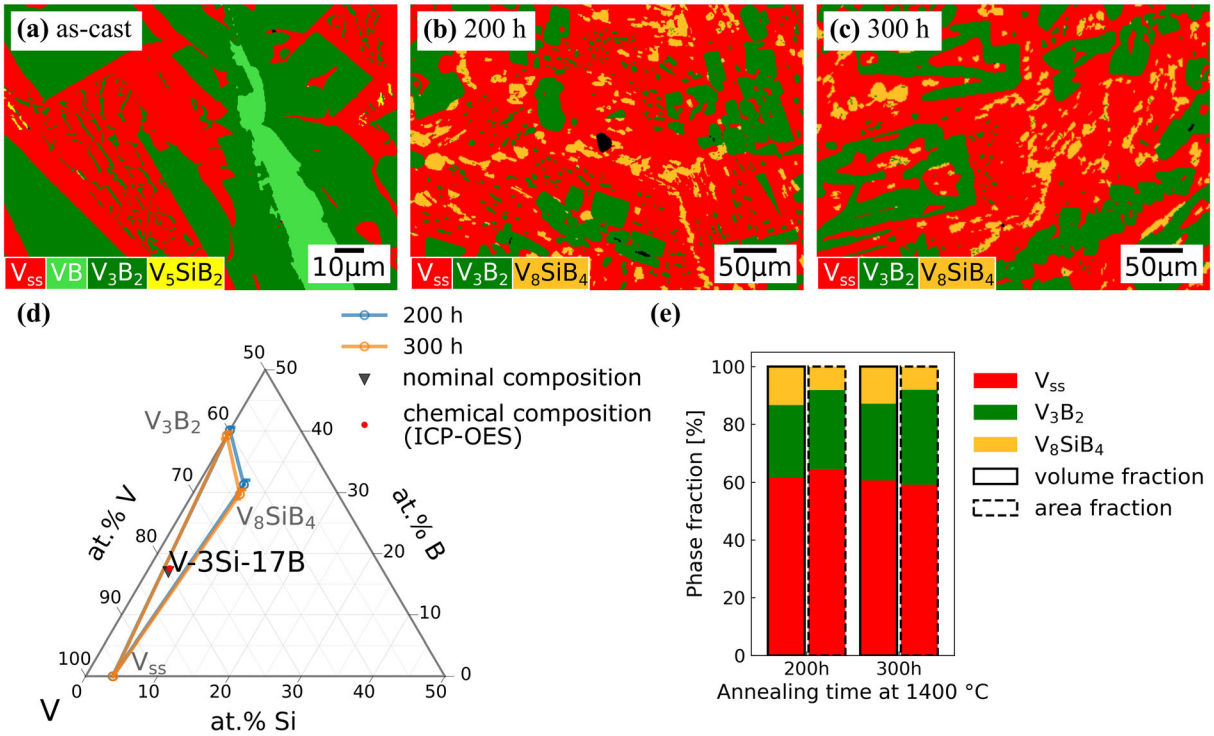


**Fig. 3** Experimental microstructures (EBSD phase mappings) of alloy V-3Si-17B in the (a) as-cast condition and after annealing for (b) 200 h and (c) 300 h. (d) The phase compositions measured by EDS (marked with open circles), where the error bars are plotted along the fixed B and Si contents for the standard deviations exceeding 0.3 at.% Si and B. (e) The evolution of phase volume and area fractions showing that the equilibrium state at 1400 °C was reached after 200 h

$V_5SiB_2$ phase in the as-cast state. After 100 h of annealing at 1400 °C, the alloy V-5Si-5B is close to the phase equilibrium because an additional 100 h of annealing did not change the phase compositions (Table 3 or Fig. 4d) or the volume and area fractions of each phase (Fig. 4e). Furthermore, as shown in Fig. 4(d), V-5Si-5B is located close to the line connecting the $V_{ss}$ and $V_8SiB_4$ phases, but the $V_3Si$ phase can still be observed after annealing, which suggests that the alloy is close to the $V_{ss}$-$V_8SiB_4$ phase region.

In the as-cast alloy V-16.5Si-3.5B, the $V_3Si$ primary phase, the coarse $V_5SiB_2$ phase and the $V_{ss}$-$V_5SiB_2$ eutectic were observed (Fig. 5a). After annealing at 1400 °C for 100 h, discontinuous regions consisting of the $V_{ss}$ and $V_8SiB_4$ phases were observed in the $V_3Si$ matrix phase (Fig. 5b). The coexistence of the $V_{ss}$, $V_3Si$ and $V_8SiB_4$ phases after the heat treatment was confirmed by XRD (Table 2). Like alloy V-5Si-5B, alloy V-16.5Si-3.5B is also located within the three-phase field of $V_{ss}$-$V_3Si$-$V_8SiB_4$ (Fig. 5d). The difference between these two alloys is, however, that the most abundant phase in the annealed alloys V-5Si-5B is the $V_{ss}$ phase, while in the annealed alloys V-16.5Si-3.5B it is the $V_3Si$ phase. Similarly, the phase equilibrium must be reached in alloy V-16.5Si-3.5B annealed at 1400 °C after 100 h according to the evolution of phase volume and area fractions (Fig. 5e), where the changes from 100 h to 200 h are negligible. Thus, the annealed alloys V-5Si-5B and V-16.5Si-3.5B were used to determine the phase field of $V_{ss}$-$V_3Si$-$V_8SiB_4$.

### *3.1.4 Phase Field of $V_3Si$-$V_8SiB_4$-$V_5SiB_2$*

In the as-cast alloy V-18.5Si-6.5B, the $V_3Si$-$V_5SiB_2$ and $V_{ss}$-$V_5SiB_2$ eutectics were observed (Fig. 6a). After annealing at 1400 °C for 100 h, the $V_{ss}$ phase had almost disappeared, while the $V_8SiB_4$ phase had formed close to the $V_5SiB_2$ phase within a $V_3Si$ matrix (Fig. 6b). An additional 100 h annealing did not change the microstructure significantly (Fig. 6c), although the $V_{ss}$ phase, which has a negligible area fraction (Fig. 6e) and cannot be detected by XRD (Table 2), was detected by EBSD. Thus, the annealed alloys V-18.5Si-6.5B must be very close to

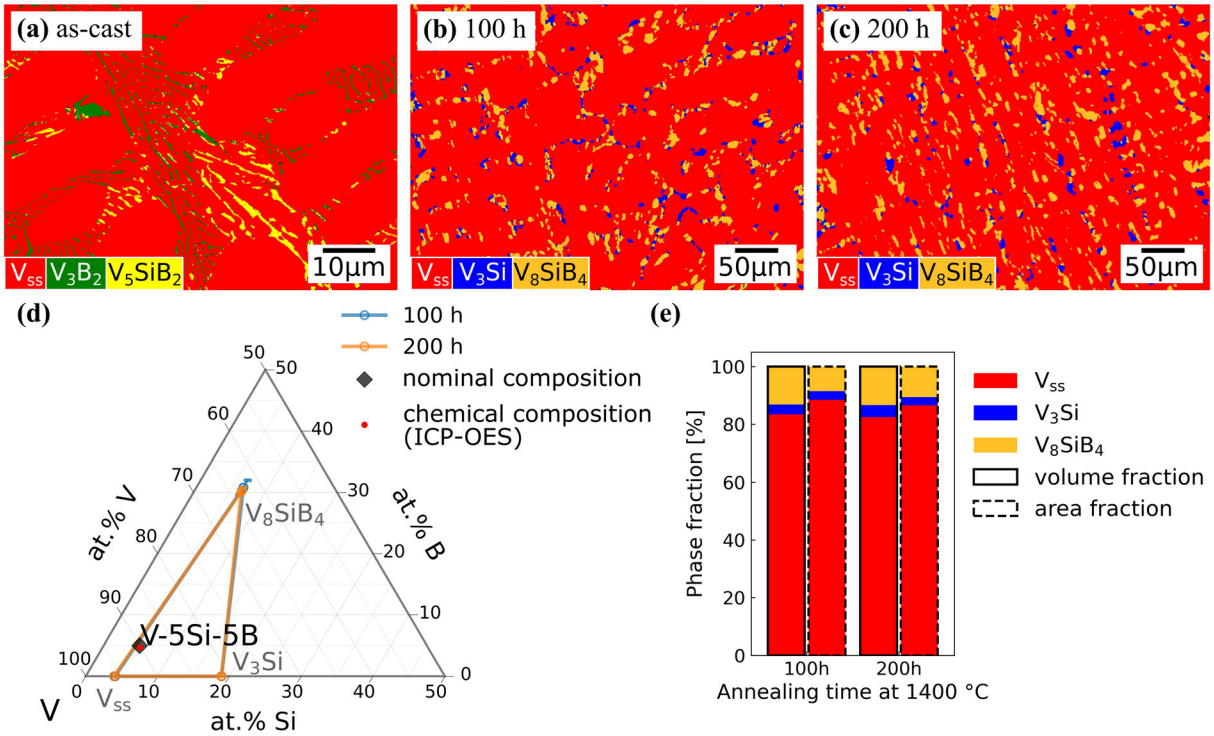


**Fig. 4** Experimental microstructures (EBSD phase mappings) of alloy V-5Si-5B in the (a) as-cast condition and after annealing for (b) 100 h and (c) 200 h. (d) The phase compositions measured by EDS (marked with open circles), where the error bars are plotted along the fixed B and Si contents for the standard deviations exceeding 0.3 at.% Si and B. (e) The evolution of phase volume and area fractions showing that the equilibrium state at 1400 °C was reached after 100 h

the equilibrium state between $V_3Si$, $V_8SiB_4$ and $V_5SiB_2$ phases. The measured phase compositions (Table 3 or Fig. 6d) were used to determine the phase field of $V_3Si$-$V_8SiB_4$-$V_5SiB_2$.

### *3.1.5 Phase Field of $V_3Si$-$V_5SiB_2$*

The as-cast alloy V-20Si-6.5B consists of the continuous $V_3Si$ phase, the coarse $V_5SiB_2$ phase and the $V_{ss}$-$V_5SiB_2$ eutectic (Fig. 7a). The continuous $V_3Si$ phase should be the primary phase according to the reported liquidus projection.[28,29] After annealing at 1400 °C for 100 h and 300 h, the $V_{ss}$ phase had disappeared and the $V_5SiB_2$ phase had been distributed within a $V_3Si$ matrix (Fig. 7b and c). The observed microstructures agree well with the XRD results (Table 2). Furthermore, the phase compositions of $V_3Si$ and $V_5SiB_2$ were measured by EDS and the corresponding results (Table 3) are plotted in Fig. 7(d), where the compositional position of alloy V-20Si-6.5B is located close to the line connecting the average phase compositions of $V_3Si$ and $V_5SiB_2$. As the annealing time was increased from 100 h to 300 h, no significant change in phase volume and area fraction (Fig. 7e) was detected, indicating that the equilibrium state must have been reached after 100 h. Thus, the annealed alloys V-20Si-6.5B confirm the existence of $V_3Si$-$V_5SiB_2$ phase field at 1400 °C.

### *3.1.6 Phase Field of $V_3Si$-$V_5SiB_2$-$V_5Si_3$*

According to the XRD results (Table 2), the $V_3Si$, tetragonal $V_5Si_3$ and $V_5SiB_2$ phases exist in the as-cast alloy V-26Si-3B. However, the EBSD results (Fig. 8a) show some unexpected phases, the hexagonal $V_5Si_3$ and $V_2C$ phases with negligible volume fractions in the as-cast state. In the annealed alloys V-26Si-3B, the $V_3Si$, tetragonal and hexagonal $V_5Si_3$ and $V_5SiB_2$ phases were observed (Fig. 8b and c). The hexagonal $V_5Si_3$ phase shown in EBSD phase mappings was detected by combining the EBSD and EDS mapping, because the EBSD method cannot distinguish between the hexagonal $V_5Si_3$[23,30] and

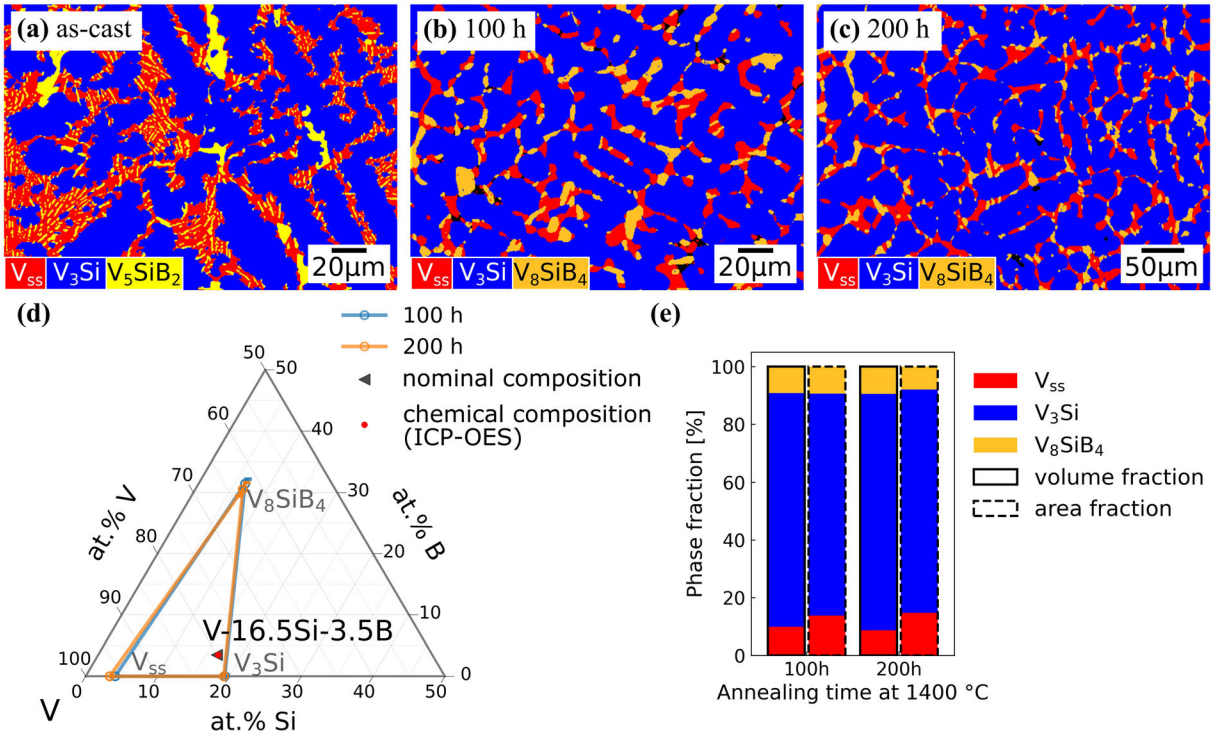


**Fig. 5** Experimental microstructures (EBSD phase mappings) of alloy V-16.5Si-3.5B in the (a) as-cast condition and after annealing for (b) 100 h and (c) 200 h. (d) The phase compositions measured by EDS (marked with open circles), where the error bars are plotted along the fixed B and Si contents for the standard deviations exceeding 0.3 at.% Si and B. (e) The evolution of phase volume and area fractions showing that the equilibrium state at 1400 °C was reached after 100 h

$V_5Si_3B$[8,9] phases due to their similar crystal structures and lattice parameters. Fortunately, the EDS elemental mappings can indeed help to distinguish these two phases due to their different compositions (Fig. 8d and e). In agreement with EBSD and EDS, XRD detected both the tetragonal and hexagonal $V_5Si_3$ phases after the heat treatment (Table 2).

According to the investigation of the V-Si-B system at 1450 °C [8] and 1600 °C,[9] the $V_5Si_3$ phase should have a tetragonal crystal structure (*I4/mcm*). However, a hexagonal $V_5Si_3$ phase (*$P6_3$/mcm*) can be stabilized by a small amount of carbon (0.1-0.2 wt.%) .[23] Thus, the existence of a hexagonal $V_5Si_3$ phase could be an indicator of a small amount of carbon contamination, which could originate from the raw materials or the fabrication process and was confirmed by the combustion analysis of carbon ($0.013 \pm 0.004$ wt.%) for the as-cast alloy. This finding agrees well with the occurrence of the $V_2C$ phase suggested by EBSD in the as-cast alloy (Fig. 8a).

The phase compositions of the $V_3Si$, tetragonal $V_5Si_3$ and $V_5SiB_2$, measured by EDS in the annealed alloys V-26Si-3B (Table 3), are shown in a ternary diagram (Fig. 8f) and were used to calculate the phase volume fractions. The calculated volume fraction or the measured area fraction of each phase remained almost constant in alloy V-26Si-3B annealed at 1400 °C when the annealing time was increased from 100 h to 200 h (Fig. 8g). Thus, alloy V-26Si-3B must have reached the equilibrium state at 1400 °C after 100 h. Since the volume fractions of the hexagonal $V_5Si_3$ phase are much smaller than those of the other three phases in the annealed alloys (Fig. 8g), the compositions of the other three phases are very close to the phase equilibrium of the $V_3Si$-$V_5Si_3$-$V_5SiB_2$ phase field. Thus, the annealed alloys V-26Si-3B were used to determine the phase field of $V_3Si$-$V_5Si_3$-$V_5SiB_2$.

### *3.1.7 Phase Field of VB-$V_3B_2$-$V_8SiB_4$*

The microstructure of the as-cast alloy V-1Si-40B (Fig. 9a) indicates that the VB primary phase was followed by the formation of the $V_3B_2$ phase, and the formation of the $V_{ss}$-$V_3B_2$ and $V_{ss}$-$V_5SiB_2$ eutectics in agreement with the

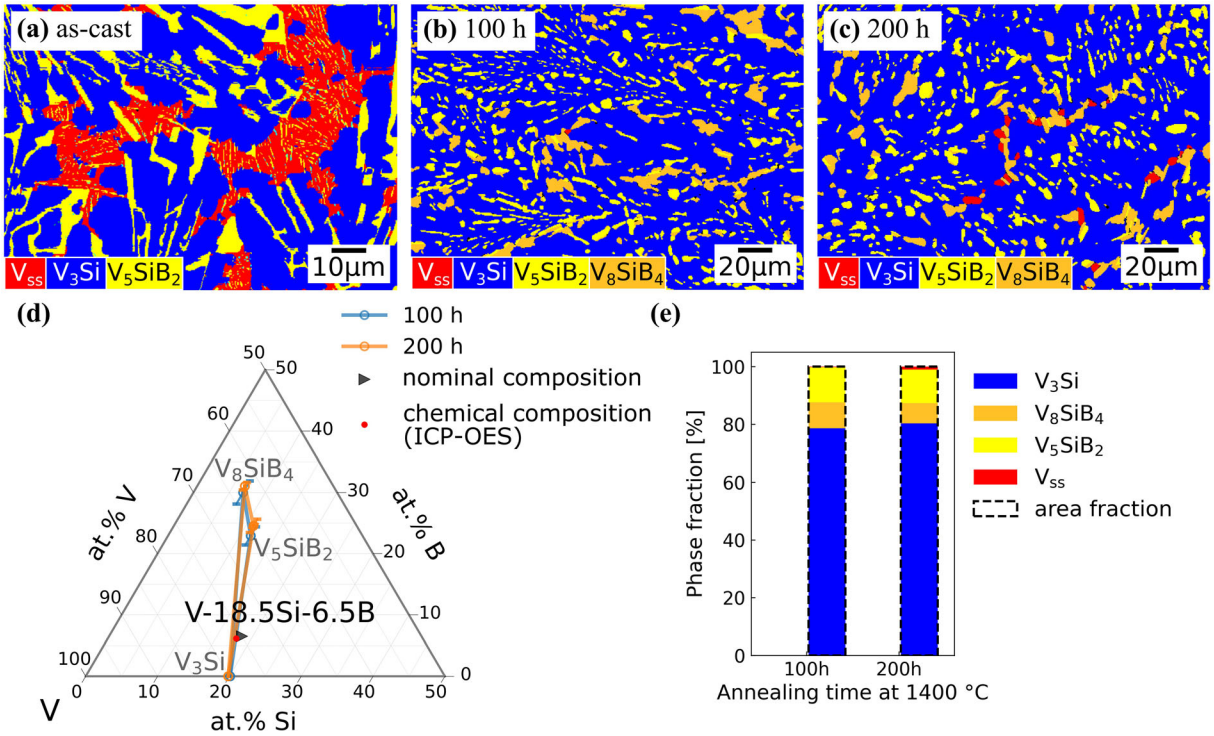


**Fig. 6** Experimental microstructures (EBSD phase mappings) of alloy V-18.5Si-6.5B in the (a) as-cast condition and after annealing for (b) 100 h and (c) 200 h. (d) The phase compositions measured by EDS (marked with open circles), where the error bars are plotted along the fixed B and Si contents for the standard deviations exceeding 0.3 at.% Si and B. (e) The evolution of phase area fractions showing that the equilibrium state at 1400 °C was almost reached after 100 h

reported liquidus projection.[28,29] Annealing at 1400 °C for 200 h caused the $V_3B_2$ phase adjacent to the VB phase to grow and separate the VB phase from the newly formed $V_8SiB_4$ phase (Fig. 9b). As the annealing time increased, the $V_{ss}$ phase further dissolved (Fig. 9c). Consistent with the observed microstructures (Fig. 9b and c), the XRD results suggest a negligible volume or area fraction for the $V_{ss}$ phase in the annealed alloys (Table 2). Neglecting the presence of the $V_{ss}$ phase, the measured phase compositions (Table 3 or Fig. 9d) were used to calculate the evolution of the phase volume fractions (Fig. 9e), which can indicate that the phase equilibria after 300 h annealing was almost reached. Thus, the alloy V-1Si-40B annealed at 1400 °C for 300 h was used to determine the phase field of VB-$V_3B_2$-$V_8SiB_4$ in this work.

### *3.1.8 Phase Field of VB-$V_5SiB_2$-$V_5Si_3$*

The as-cast alloy V-20Si-20B consists of the VB primary phase, the tetragonal $V_5Si_3$ phase, the $V_5SiB_2$ phase and the $V_3Si$-$V_5SiB_2$ eutectic (Fig. 10a). After annealing at 1400 °C for 200 h, the $V_3Si$ phase had disappeared, while the $V_5SiB_2$ phase had formed separating the VB phase from the other phases (Fig. 10b).

Similar to the annealed alloys V-26Si-3B, not only the tetragonal $V_5Si_3$ phase, but also the hexagonal $V_5Si_3$ phase were identified by combining the EBSD phase mappings and the B elemental mappings in the annealed alloys V-20Si-20B (Fig. 10b–e). As mentioned for the annealed alloys V-26Si-3B, the presence of the hexagonal $V_5Si_3$ phase may indicate a small amount of carbon contamination in the alloys V-20Si-20B, which was also confirmed by the combustion analysis of carbon (0.034 wt.%, here only one measurement was performed) for the as-cast alloy. Thus, carbon, in negligible amounts, stabilized an additional hexagonal $V_5Si_3$ phase in the phase fields containing the tetragonal $V_5Si_3$ phase, namely VB-$V_5SiB_2$-$V_5Si_3$ and $V_3Si$-$V_5SiB_2$-$V_5Si_3$. However, it did not influence the other equilibrium phase fields investigated in this work.

Neglecting the hexagonal $V_5Si_3$ phase, the calculated evolution of phase volume fractions in the annealed alloys V-20Si-20B can indicate the phase equilibrium state after the annealing at 1400 °C for 200 h (Fig. 10g). By contrast, the area fraction of the VB phase had decreased

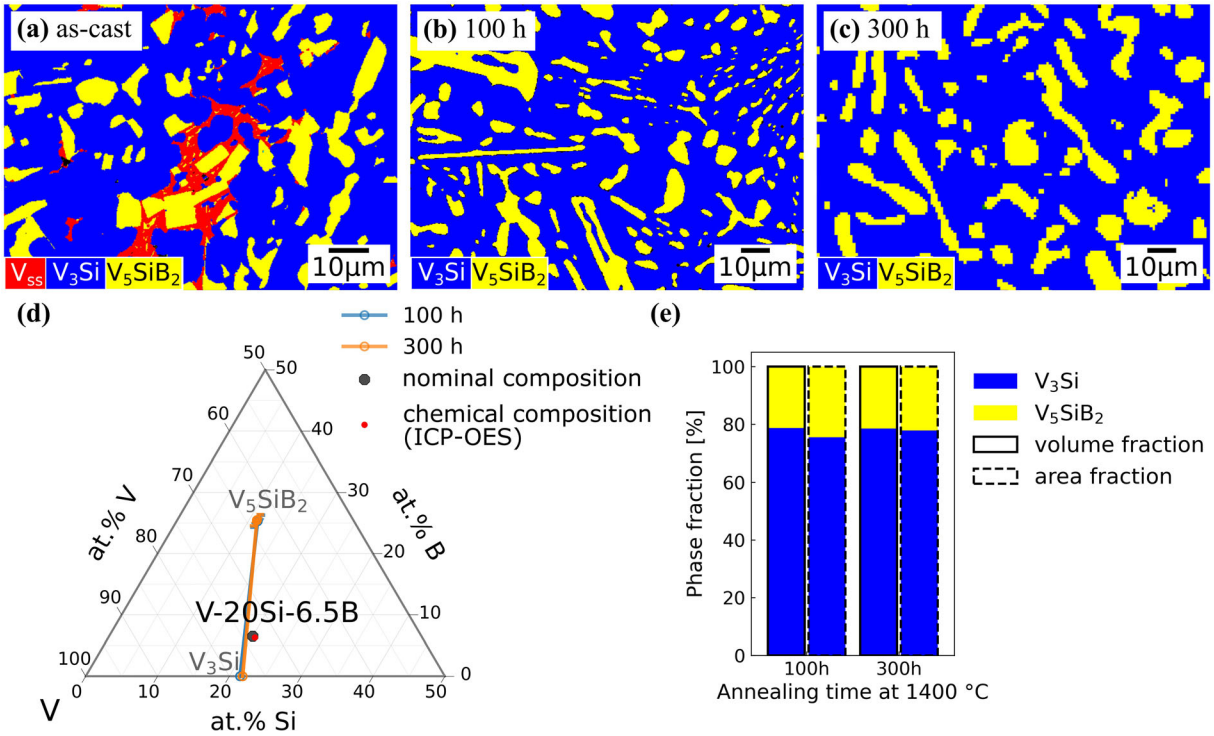


**Fig. 7** Experimental microstructures (EBSD phase mappings) of alloy V-20Si-6.5B in the (a) as-cast condition and after annealing for (b) 100 h and (c) 300 h. (d) The phase compositions measured by EDS (marked with open circles), where the error bars are plotted along the fixed B and Si contents for the standard deviations exceeding 0.3 at.% Si and B. (e) The evolution of phase volume and area fractions showing that the equilibrium state at 1400 °C was reached after 100 h

significantly from 200 h to 300 h, while the area fraction of the $V_5SiB_2$ phase had increased (Fig. 10g). However, this observation might be related to the insufficient area scanned by EBSD (Fig. 10b and c). As in the annealed alloys V-26Si-3B, the negligible hexagonal $V_5Si_3$ phase in the annealed alloys V-20Si-20B has no significant effect on the phase equilibrium of the VB-$V_5SiB_2$-$V_5Si_3$ phase field, and therefore the measured compositions of the VB, $V_5SiB_2$ and $V_5Si_3$ phases (Table 3) were used to determine the phase field of VB-$V_5SiB_2$-$V_5Si_3$.

### *3.1.9 Phase Field of VB-$V_8SiB_4$-$V_5SiB_2$*

According to the microstructure of the as-cast alloy V-7Si-33B (Fig. 11a) and the reported liquidus projection,[28,29] the solidification sequence in the as-cast alloy V-7Si-33B should be the VB primary phase, the $V_5SiB_2$ phase, the $V_5SiB_2$-$V_3Si$ and $V_{ss}$-$V_5SiB_2$ eutectics. The presence of the $V_3B_2$ and $V_8SiB_4$ phases suggested by EBSD (Fig. 11a) in the as-cast state cannot be confirmed by XRD (Table 2) due to their negligible phase fractions. After annealing at 1400 °C for 200 h and 300 h, the $V_{ss}$ phase and the eutectics had disappeared, while the $V_3B_2$ phase had precipitated along the boundaries between the VB and $V_5SiB_2$ phases (Fig. 11b and c). Meanwhile, small globular $V_8SiB_4$ phase was observed mostly near the boundaries between the $V_3B_2$ and $V_5SiB_2$ phases. The residual $V_3Si$ phase is surrounded by the $V_5SiB_2$ phase (Fig. 11b and c). Thus, the annealed alloys V-7Si-33B located in the phase field of VB-$V_8SiB_4$-$V_5SiB_2$ (Fig. 11d) had not reached the equilibrium state. However, the VB, $V_5SiB_2$, $V_8SiB_4$ phases observed after annealing still agree with the existence of the corresponding three-phase field of these phases as a consequence of the existence of the VB-$V_3B_2$-$V_8SiB_4$, $V_3Si$-$V_8SiB_4$-$V_5SiB_2$, $V_3Si$-$V_5SiB_2$ and VB-$V_5SiB_2$-$V_5Si_3$ phase fields, which were confirmed above.

The formation of the $V_3B_2$ phase in the annealed alloys V-7Si-33B (Fig. 11b and c) can indicate that it is difficult to reach equilibrium in the phase field of VB-$V_8SiB_4$-$V_5SiB_2$ because of the reaction and diffusion kinetics. To estimate the phase field of VB-$V_8SiB_4$-$V_5SiB_2$, the VB-$V_8SiB_4$ phase field was assumed as a coexistence line in

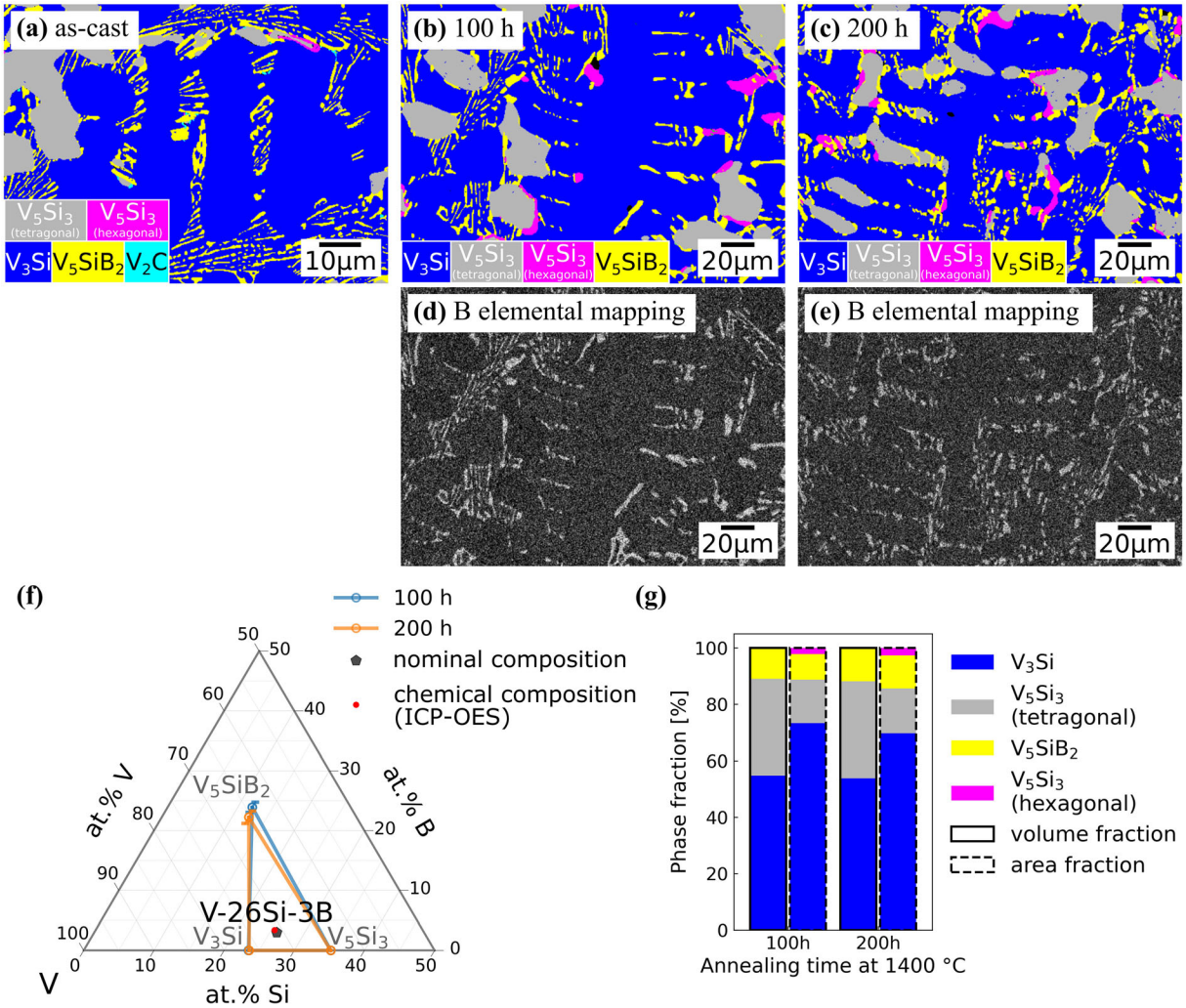


**Fig. 8** Experimental microstructures (EBSD phase mappings) of alloy V-26Si-3B in the (a) as-cast condition and after annealing for (b) 100 h and (c) 200 h. (d)-(e) the B elemental mappings of the annealed alloys. (f) The phase compositions measured by EDS (marked with open circles), where the error bars are plotted along the fixed B and Si contents for the standard deviations exceeding 0.3 at.% Si and B. (g) The evolution of phase volume and area fractions showing that the equilibrium state at 1400 °C was reached after 100 h

this work, while the composition of the $V_5SiB_2$ phase of this phase field can be determined using the annealed alloys V-3Si-38B as discussed below.

In the as-cast alloy V-3Si-38B, the VB primary phase, the $V_3B_2$ phase, the $V_8SiB_4$ phase and the $V_{ss}$-$V_5SiB_2$ eutectic were observed (Fig. 12a) in agreement with the XRD analysis (Table 2). The precipitation of the $V_8SiB_4$ phase in the as-cast state is not expected based on the reported liquidus projection,[28,29] but can be caused by the slow cooling rate in the levitation melter. After 100 h of annealing at 1400 °C, the $V_3B_2$ phase had increased in size and separated the VB phase and the $V_8SiB_4$ phase (Fig. 12b). As the annealing time was increased from 100 to 200 h, the $V_3Si$ and $V_{ss}$ phases dissolved (Fig. 12c), and the particles of the $V_5SiB_2$ phase were surrounded by the $V_8SiB_4$ phase. Despite the fact that the alloy V-3Si-38B did not reach a phase equilibrium state at 1400 °C after annealing for 200 h, the measured phase composition of $V_5SiB_2$ in the alloy V-3Si-38B annealed at 1400 °C for 200 h corresponds to the composition of the $V_5SiB_2$ phase in the phase field of VB-$V_8SiB_4$-$V_5SiB_2$ assuming the VB-$V_8SiB_4$ coexistence line (Fig. 12d).

### 3.2 Constructing the Isothermal Section at 1400 °C

Based on the findings discussed above and the measured phase compositions of the alloys marked in Fig. 13, the isothermal section at 1400 °C was assessed as shown in Fig. 13. It should be noted that the phase field of VB-$V_8SiB_4$ is assumed as a coexisting line. Compared to the isothermal section of V-VB-$V_5Si_3$ proposed by Nunes et al.[9] at 1600 °C (Fig. 1), the presence of the recently found

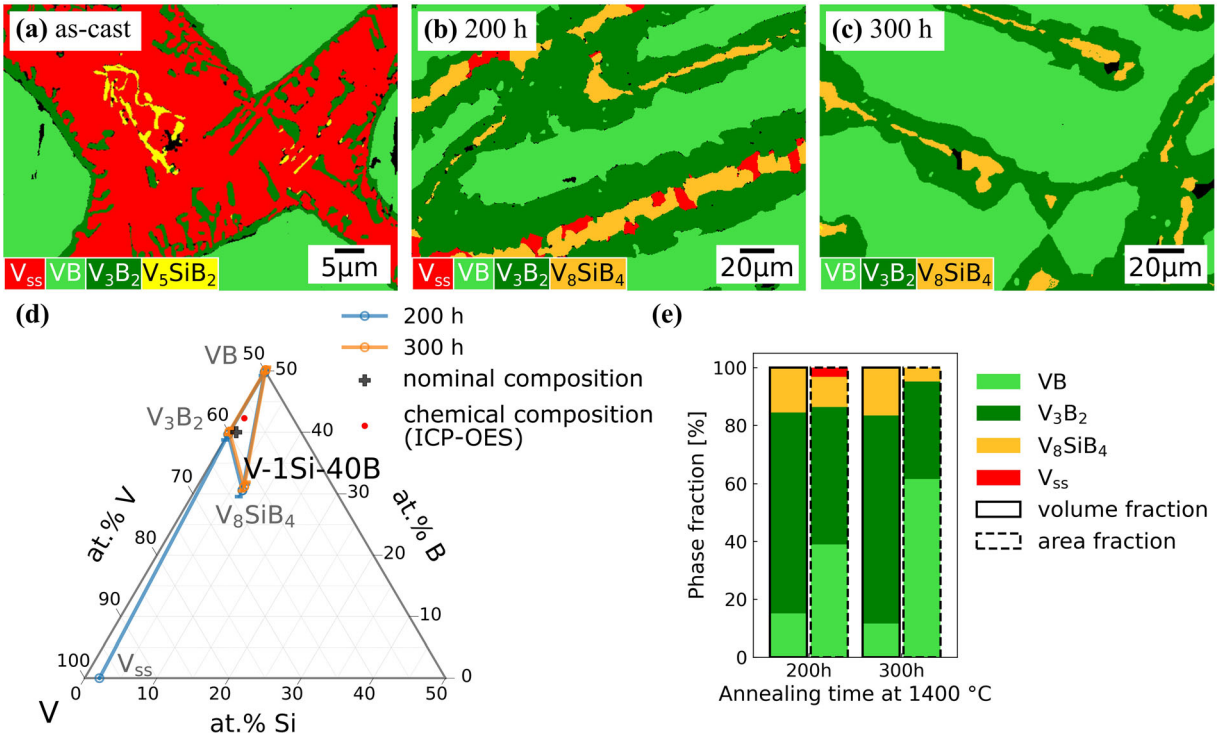


**Fig. 9** Experimental microstructures (EBSD phase mappings) of alloy V-1Si-40B in the (a) as-cast condition and after annealing for (b) 200 h and (c) 300 h. (d) The phase compositions measured by EDS (marked with open circles), where the error bars are plotted along the fixed B and Si contents for the standard deviations exceeding 0.3 at.% Si and B. (e) The evolution of phase volume fractions showing that the equilibrium state at 1400 °C was almost reached after 300 h, even if the negligible $V_{ss}$ was detected by XRD

$V_8SiB_4$ phase [17] is responsible for the microstructural difference at 1400 °C. The $V_5SiB_2$ phase field at 1600 °C (Fig. 1) is partially replaced by the phase field of $V_8SiB_4$-$V_5SiB_2$ at 1400 °C (Fig. 13). Accordingly, it divides the $V_5SiB_2$-$V_3Si$ phase field at 1600 °C into three phase fields at 1400 °C, i.e., the $V_3Si$-$V_8SiB_4$, $V_3Si$-$V_8SiB_4$-$V_5SiB_2$ and $V_3Si$-$V_5SiB_2$ phase fields. Similarly, the VB-$V_5SiB_2$ phase field at 1600 °C is divided into VB-$V_8SiB_4$-$V_5SiB_2$ and VB-$V_5SiB_2$ phase fields. Furthermore, the $V_5SiB_2$ phase of the $V_{ss}$-$V_3B_2$-$V_5SiB_2$, $V_{ss}$-$V_3Si$-$V_5SiB_2$ and VB-$V_3B_2$-$V_5SiB_2$ phase fields at 1600 °C (Fig. 1) is replaced by the $V_8SiB_4$ phase (Fig. 13). Like the binary coexisting line of $V_{ss}$-$V_5SiB_2$ at 1600 °C, the phase field of $V_{ss}$-$V_8SiB_4$ is still represented by a coexisting line at 1400 °C.

### 3.3 Comparison to the Binary Phase Diagrams

The measured B content of the $V_3B_2$ phase in Fig. 13 is comparable to the reported binary V-B phase diagram,[15] which indicates an acceptable accuracy of the EDS measurement for a V-boride phase. By contrast, the EDS results of V-silicide phases ($V_3Si$ and $V_5Si_3$) deviate from the reported V-Si system.[13] As shown in Fig. 14, the measured Si content of the V-rich $V_3Si$ phase in the $V_{ss}$-$V_3Si$-$V_8SiB_4$ phase field in this work is around 4 at.% lower than that reported in the binary V-Si phase diagram ,[13] while the measured Si content of the Si-rich $V_3Si$ phase in the $V_3Si$-$V_5SiB_2$-$V_5Si_3$ phase field is around 1 at.% lower. Furthermore, the measured Si content of the $V_5Si_3$ phase is around 2.5 at.% lower than that reported in the binary V-Si phase diagram .[13] Compared to the EDS results in this work, the phase compositions of $V_3Si$ and $V_5Si_3$ measured by Nunes et al. [9] agree well with the

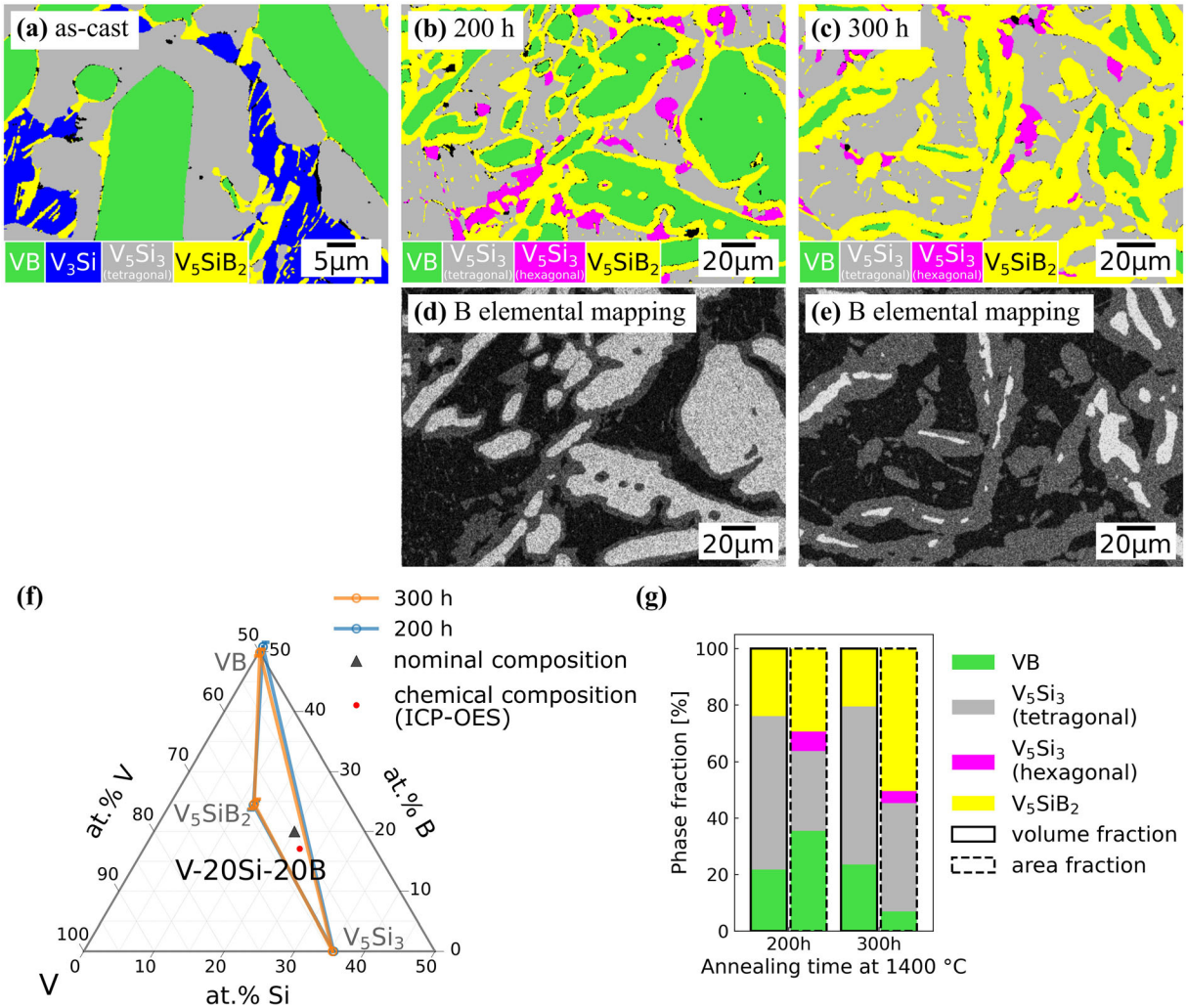


**Fig. 10** Experimental microstructures (EBSD phase mappings) of alloy V-20Si-20B in the (a) as-cast condition and after annealing for (b) 200 h and (c) 300 h. (d)-(e) The B elemental mappings of the annealed alloys. (f) The phase compositions measured by EDS (marked with open circles), where the error bars are plotted along the fixed B and Si contents for the standard deviations exceeding 0.3 at.% Si and B. (g) The evolution of phase volume and area fractions showing that the equilibrium state at 1400 °C was reached after 200 h

binary V-Si phase diagram (Fig. 14). However, the measured composition of $V_{ss}$ at 1400 °C in this work agrees well with the binary V-Si phase diagram ,[13] while the composition measured by Nunes et al. [9] at 1600 °C is around 2 at.% higher than the one in the V-Si binary phase diagram (Fig. 14).

To confirm the validity of the EDS results for the $V_3Si$ phase investigated in this work, the relationship between the lattice parameter and the phase composition of $V_3Si$ determined by Jorda and Muller [31] was used. This relationship is shown as a dashed line in Fig. 15, where the experimental results obtained in the present work are scattered around that line (black symbols). According to this relationship,[31] the compositions of the $V_3Si$ phase in both the $V_{ss}$-$V_3Si$-$V_8SiB_4$ and the $V_3Si$-$V_5SiB_2$-$V_5Si_3$ phase fields were calculated using the lattice parameters obtained by XRD (Fig. 15) and are indeed comparable to the EDS results as shown in Fig. 14.

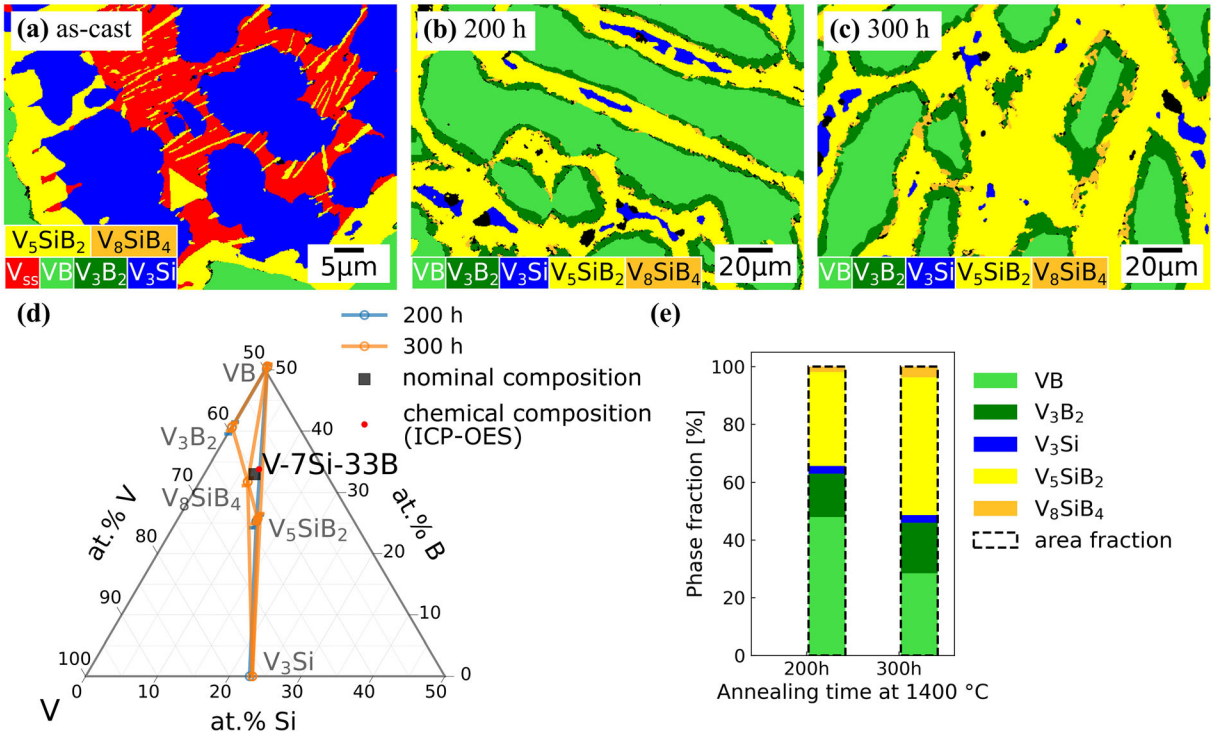


**Fig. 11** Experimental microstructures (EBSD phase mappings) of alloy V-7Si-33B in the (a) as-cast condition and after annealing for (b) 200 h and (c) 300 h. (d) The phase compositions measured by EDS (marked with open circles), where the error bars are plotted along the fixed B and Si contents for the standard deviations exceeding 0.3 at.% Si and B. (e) The evolution of phase volume and area fractions showing that the equilibrium state at 1400 °C was not be reached even after 300 h

For additional confirmation, an alloy with the nominal composition of V-37.5Si corresponding to the stoichiometric composition of the $V_5Si_3$ phase was produced via arc-melting. As expected, the as-cast alloy V-37.5Si is almost a single-phase alloy, except for the $V_3Si$ phase and the hexagonal $V_5Si_3$ phase with negligible area fractions (Fig. 16a and b). The chemical composition of the alloy determined by ICP-OES, i.e., V-36.4 ± 0.3 Si, is almost identical to the phase composition of $V_5Si_3$ based on EDS, i.e., V-35.9 ± 0.2 Si.

## 4 Summary

The phase equilibria in the V-rich of the V-Si-B system at 1400 °C were experimentally investigated and then the isothermal section was constructed. The stabilities of both the $V_5SiB_2$ and $V_8SiB_4$ ternary phases were confirmed. Compared to the isothermal section at 1600 °C,[9] the appearance of the $V_8SiB_4$ phase at 1400 °C has the following consequences:

1. The solubility range of the $V_5SiB_2$ phase decreases as the temperature decreases from 1600 to 1400 °C;

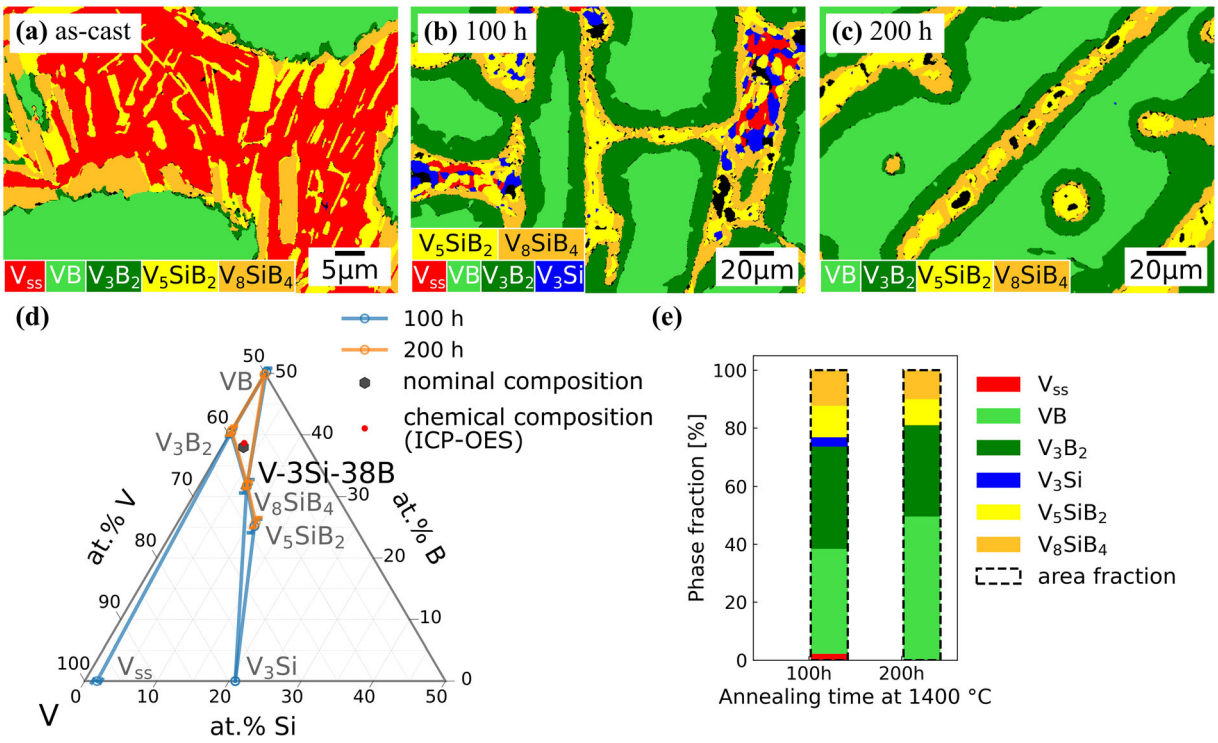


**Fig. 12** Experimental microstructures (EBSD phase mappings) of alloy V-3Si-38B in the (a) as-cast condition and after annealing for (b) 100 h and (c) 200 h. (d) The phase compositions measured by EDS (marked with open circles), where the error bars are plotted along the fixed B and Si contents for the standard deviations exceeding 0.3 at.% Si and B. (e) The evolution of phase volume and area fractions showing that the equilibrium state at 1400 °C was not be reached after 200 h

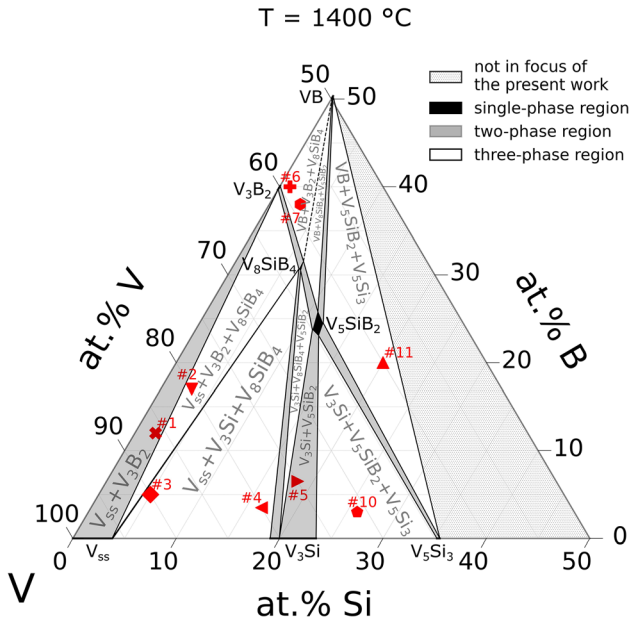


**Fig. 13** The isothermal section of the V-rich corner of the V-Si-B system at 1400 °C based on the marked alloys, where the phase field of VB-$V_8SiB_4$ is assumed as a coexisting line

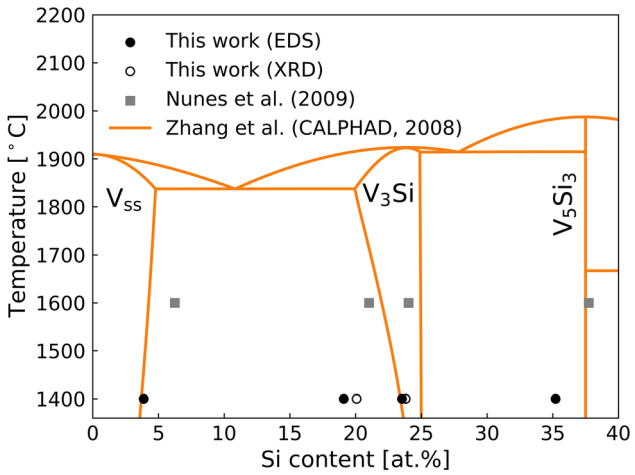


**Fig. 14** The phase compositions of $V_{ss}$, $V_3Si$ and $V_5Si_3$ measured at 1400 °C (this work) and measured by Nunes et al. [9] at 1600 °C are compared to those of the binary V-Si phase diagram calculated by Zhang et al. [14], where the open symbols represent the compositions calculated according to the relationship between the lattice parameter and the phase composition of $V_3Si$ reported by Jorda and Muller [31] shown in Fig. 15

2. The $V_3Si$-$V_5SiB_2$ phase field at 1600 °C is divided into the $V_3Si$-$V_8SiB_4$, $V_3Si$-$V_8SiB_4$-$V_5SiB_2$ and $V_3Si$-$V_5SiB_2$ phase fields at 1400 °C, while the VB-$V_5SiB_2$ phase field at 1600 °C is divided into VB-$V_8SiB_4$-$V_5SiB_2$ and VB-$V_5SiB_2$ phase fields;
3. The $V_{ss}$-$V_3B_2$-$V_5SiB_2$, $V_{ss}$-$V_3Si$-$V_5SiB_2$ and VB-$V_3B_2$-$V_5SiB_2$ three-phase fields at 1600 °C are replaced by the $V_{ss}$-$V_3B_2$-$V_8SiB_4$, $V_{ss}$-$V_3Si$-$V_8SiB_4$ and VB-$V_3B_2$-$V_8SiB_4$ three-phase fields at 1400 °C, respectively.

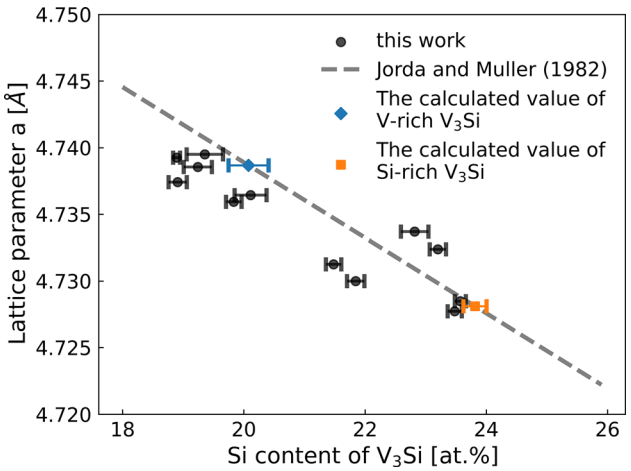


**Fig. 15** The relationship between the lattice parameter and the phase composition of $V_3Si$ compared to the dashed line reported by Jorda and Muller [31]. Using this relationship (dashed line), the phase compositions of the V-rich and Si-rich $V_3Si$ were calculated

**Acknowledgments** This work was supported by the Deutsche Forschungsgemeinschaft (DFG), Germany, under project number 410338871. The authors would like to thank C. Thomas (ER−C−1, FZ Jülich) for providing access to the arc-melter, Dr. W. Behr (ZEA−1, FZ Jülich) and T. Koppitz (ZEA−1, FZ Jülich) for their assistance in heat treatment, Dr. E. Wessel (IEK−2, FZ Jülich) and Dr. D. Grüner (IEK−2, FZ Jülich) for their assistance in SEM investigation as well as EBSD and EDS measurements, M. Ziegner (IEK−2, FZ Jülich) for supporting the XRD analysis. W. G. Yang thanks Dr. D. Sergeev (NETZSCH Analyzing & Testing) for fruitful discussion about phase diagrams.

## References

1. J.A. Lemberg and R.O. Ritchie, Mo-Si-B Alloys for Ultrahigh-Temperature Structural Applications, *Adv. Mater.*, 2012, **24**, p 3445.
2. P. Jain and K.S. Kumar, Dissolved Si in Mo and its Effects on the Properties of Mo-Si-B Alloys, *Scripta Mater*, 2010, **62**, p 1.
3. F.A. Rioult, S.D. Imhoff, R. Sakidja, and J.H. Perepezko, Transient Oxidation of Mo-Si-B Alloys: Effect of the Microstructure Size Scale, *Acta Mater*, 2009, **57**, p 4600.
4. I. Grammenos and P. Tsakiropoulos, Study of the Role of Hf, Mo and W Additions in the Microstructure of Nb-20Si Silicide Based Alloys, *Intermetallics*, 2011, **19**, p 1612.
5. M. Wenderoth, R. Völkl, S. Vorberg, Y. Yamabe-Mitarai, H. Harada, and U. Glatzel, Microstructure, Oxidation Resistance and High-Temperature Strength of $\gamma'$ Hardened Pt-Base Alloys, *Intermetallics*, 2007, **15**, p 539.
6. J. Williams and M. Akinc, Oxidation Behavior of $V_5Si_3$ Based Materials, *Intermetallics*, 1998, **6**, p 269.

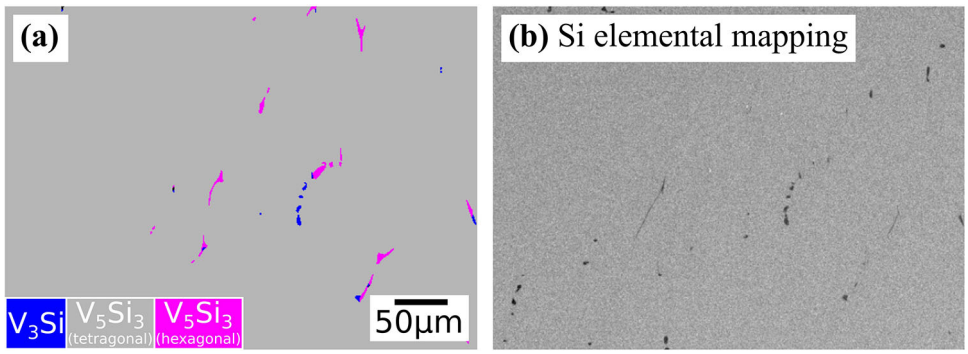


**Fig. 16** (a) The microstructure (EBSD phase mapping with a scanning step size of 0.88 µm) of the as-cast alloy V-37.5Si. (b) The corresponding Si elemental mapping. The alloy consists of almost only the tetragonal $V_5Si_3$ phase

7. M. Krüger, High Temperature Compression Strength and Oxidation of a V-9Si-13B Alloy, *Scripta Mater*, 2016, **121**, p 75.
8. H. Kudielka, H. Nowotny, and G. Findeisen, Untersuchungen in den Systemen: V-B, Nb-B, V-B-Si und Ta-B-Si, *Mon. Chem. Verwandte Teile And. Wiss.*, 1957, **88**, p 1048.
9. C.A. Nunes, B.B. de Lima, G.C. Coelho, and P.A. Suzuki, Isothermal Section of the V-Si-B System at 1600 °C in the V-$VSi_2$-VB Region, *J. Phase Equilib. Diffus.*, 2009, **30**, p 345.
10. H. Nowotny and A. Wittmann, Zur Struktur der Metallreichen Borid-Phase bei V, Nb und Ta, *Mon. Chem. Verwandte Teile And. Wiss.*, 1958, **89**, p 220.
11. C. Colinet and J.-C. Tedenac, First Principles Calculations of the Stability of the T2 and $D8_8$ Phases in the V-Si-B System, *Intermetallics*, 2014, **50**, p 108.
12. J.F. Smith, The Si−V (Silicon-Vanadium) System, *Bullet. Alloy Phase Diagr.*, 1981, **2**, p 42.
13. J.F. Smith, The Si−V (Silicon-Vanadium) System: Addendum, *Bullet. Alloy Phase Diagr.*, 1985, **6**, p 266.
14. C. Zhang, Y. Du, W. Xiong, H. Xu, P. Nash, Y. Ouyang, and R. Hu, Thermodynamic Modeling of the V-Si System Supported by Key Experiments, *Calphad*, 2008, **32**, p 320.
15. K.E. Spear, P.K. Liao, and J.F. Smith, The B-V (Boron-Vanadium) System, *J. Ph. Equilib.*, 1987, **8**, p 447.
16. M. Krüger, V. Bolbut, F. Gang, and G. Hasemann, Microstructure Variations and Creep Properties of Novel High Temperature V-Si-B Materials, *JOM*, 2016, **68**, p 2811.
17. W.G. Yang, R.S. Touzani, G. Hasemann, M. Yazlak, M. Ziegner, B. Gorr, R. Schwaiger, and M. Krüger, $V_8SiB_4$—A New Ternary Phase in the V-Si-B System, *Intermetallics*, 2022, **151**, p 107691.
18. B.H. Toby and R.B. Von Dreele, GSAS-II: the Genesis of a Modern Open-Source All Purpose Crystallography Software Package, *J. Appl. Crystallogr.*, 2013, **46**, p 544.
19. G.S. Pawley, Unit-Cell Refinement from Powder Diffraction Scans, *J. Appl. Crystallogr.*, 1981, **14**, p 357.
20. A. Belsky, M. Hellenbrandt, V.L. Karen, and P. Luksch, New developments in the Inorganic Crystal Structure Database (ICSD): Accessibility in Support of Materials Research and Design, *Acta Crystallogr. B*, 2002, **58**, p 364.
21. H. Kohlmann, C. Hein, R. Kautenburger, T.C. Hansen, C. Ritter, and S. Doyle, Crystal Structure of Monoclinic Samarium and Cubic Europium Sesquioxides and Bound Coherent Neutron Scattering Lengths of the Isotopes 154Sm and 153Eu, *Z. Krist. Crystall. Mater.*, 2016, **231**, p 517.
22. J.-L. Staudenmann, The Electron Charge Distribution in $V_3Si$, *Solid State Commun.*, 1978, **26**, p 461.
23. E. Parthé, H. Nowotny, and H. Schmid, Strukturuntersuchungen an Siliziden, *Mon. Chem. Verwandte Teile And. Wiss.*, 1955, **86**, p 385.
24. A.B. Riabov, V.A. Yartys, B.C. Hauback, P.W. Guegan, G. Wiesinger, and I.R. Harris, Hydrogenation Behaviour, Neutron Diffraction Studies and Microstructural Characterisation of Boron Oxide-Doped Zr–V Alloys, *J. Alloy. Compd.*, 1999, **293–295**, p 93.
25. K.E. Spear and P.W. Gilles, Phase and Structure Relationships in the Vanadium-Boron System, *High Temp. Sci.*, 1969, **1**, p 86.
26. W.J. Lehmann and I. Shapiro, Isotopic Composition of Boron and its Atomic Weight, *Nature*, 1959, **183**, p 1324.
27. J.A. Bearden, X-ray Wavelengths, *Rev. Mod. Phys.*, 1967, **39**, p 78.
28. G. Hasemann, Experimental Study of the Liquidus Surface in the V-Rich Portion of the V-Si-B System, *J. Alloy. Compd.*, 2020, **824**, p 153843.
29. W.G. Yang, G. Hasemann, M. Yazlak, B. Gorr, R. Schwaiger, and M. Krüger, Ternary $V_{ss}$-$V_3Si$-$V_5SiB_2$ Eutectic Formation in the V-Si-B System, *J. Alloy. Compd.*, 2022, **902**, p 163722.
30. Y. Chen, A.N. Kolmogorov, D.G. Pettifor, J.-X. Shang, and Y. Zhang, Theoretical Analysis of Structural Stability of $TM_5Si_3$ Transition Metal Silicides, *Phys. Rev. B*, 2010, **82**, p 184104.
31. J.L. Jorda and J. Muller, The $V_3Si$ Phase: Type of Formation and Homogeneity Range, *J. Less Comm. Metals*, 1982, **84**, p 39.